Developmental Cell
Article

# Integrated Structural Model and Membrane Targeting Mechanism of the Human ESCRT-II Complex

Young Jun Im[1] and James H. Hurley[1,*]
[1]Laboratory of Molecular Biology, National Institute of Diabetes and Digestive and Kidney Diseases, National Institutes of Health, US Department of Health and Human Services, Bethesda, MD 20892, USA
*Correspondence: hurley@helix.nih.gov
DOI 10.1016/j.devcel.2008.04.004

## SUMMARY

**ESCRT-II plays a pivotal role in receptor downregulation and multivesicular body biogenesis and is conserved from yeast to humans. The crystal structures of two human ESCRT-II complex structures have been determined at 2.6 and 2.9 Å resolution, respectively. The complex has three lobes and contains one copy each of VPS22 and VPS36 and two copies of VPS25. The structure reveals a dynamic helical domain to which both the VPS22 and VPS36 subunits contribute that connects the GLUE domain to the rest of the ESCRT-II core. Hydrodynamic analysis shows that intact ESCRT-II has a compact, closed conformation. ESCRT-II binds to the ESCRT-I VPS28 C-terminal domain subunit through a helix immediately C-terminal to the VPS36-GLUE domain. ESCRT-II is targeted to endosomal membranes by the lipid-binding activities of both the Vps36 GLUE domain and the first helix of Vps22. These data provide a unifying structural and functional framework for the ESCRT-II complex.**

## INTRODUCTION

The ESCRT (endosomal sorting complex required for transport) machinery directs the budding of intralumenal vesicles from the limiting membrane of endosomes to form multivesicular bodies (MVBs) in yeast, insect, and animal cells (Babst, 2005; Hurley, 2008; Saksena et al., 2007; Williams and Urbe, 2007); the budding of HIV-1 and other enveloped viruses from the plasma membrane of animal cells (Bieniasz, 2006); and the membrane abscission step in cytokinesis (Carlton and Martin-Serrano, 2007; Morita et al., 2007). ESCRT-I and ESCRT-II are soluble and constitutively assembled complexes, which are targeted to the endosomal membrane by interactions with membrane-bound phosphoinositides and ubiquitinated membrane proteins (Babst, 2005; Hurley, 2008; Saksena et al., 2007; Williams and Urbe, 2007). ESCRT-III assembles into an insoluble array on the endosomal membrane and is thought to play a key role in membrane deformation (Babst, 2005; Hurley, 2008; Saksena et al., 2007; Williams and Urbe, 2007). ESCRT-III monomers are thought to be targeted to endosomes in part by interactions with ESCRT-II (Bowers et al., 2006; Langelier et al., 2006; Martin-Serrano et al., 2003; Teo et al., 2004; von Schwedler et al., 2003; Yorikawa et al., 2005), among other factors. Thus, ESCRT-II connects the upstream cargo-binding components of the system with the downstream membrane-remodeling machinery.

In yeast, ESCRT-II is required for the lysosomal degradation of the mating-factor receptor Ste2 (Babst et al., 2002), among other cargo. In *Drosophila*, the ESCRT-II subunit VPS25 acts as a tumor suppressor by promoting the degradation of the Notch and DPP receptors (Herz et al., 2006; Thompson et al., 2005; Vaccari and Bilder, 2005). In human cells, ESCRT-II is required for the degradation of internalized EGF receptors (Langelier et al., 2006; Malerod et al., 2007), the chemokine receptor CXCR4 (Malerod et al., 2007), and ferroportin (De Domenico et al., 2007). ESCRT-II has at least one clear-cut nonendosomal role in establishing the bicoid mRNA gradient (Irion and St Johnston, 2007). In another potential nonendosomal function, the subunits of human ESCRT-II associate with the ELL transcriptional elongation complex (Kamura et al., 2001), although the implications of this are largely unexplored. Furthermore, ESCRT-II is responsible for connecting MVBs to the Rab7 effector RILP (Progida et al., 2006; Wang and Hong, 2006), which in turn binds to the dynein-dynactin motor complex and may coordinate MVB biogenesis to dynein-mediated motility (Progida et al., 2007).

ESCRT-II is targeted to endosomal membranes, binds ubiquitinated cargo, and assembles with other ESCRT complexes through interdependent interactions. The N-terminal region of Vps36 contains a phosphoinositide-binding GLUE domain (Slagsvold et al., 2005; Teo et al., 2006) important for membrane targeting. The yeast Vps36 GLUE domain contains a large sequence insert comprising two Npl4-type zinc finger domains, NZF1 and NZF2. The structure of the former has been determined in complex with the C-terminal domain of yeast Vps28 (Gill et al., 2007), a subunit of ESCRT-I. However, human VPS36 lacks this domain, and the nature of its interaction with ESCRT-I is unknown. The complex of the yeast VPS36 NZF2 with its ligand, ubiquitin, has been modeled on the basis of an NMR structure of the Npl4 zinc finger bound to ubiquitin (Alam et al., 2004). Human VPS36 also binds to ubiquitin, but it does so via a nonconserved site on the GLUE domain (Alam et al., 2006; Hirano et al., 2006; Slagsvold et al., 2005).

The core of the yeast ESCRT-II complex is shaped like the letter "Y" and contains two copies of the Vps25 subunit and one copy each of the Vps22 and Vps36 subunits (Hierro et al., 2004; Teo et al., 2004). The N termini of the Vps22 and Vps36

**Table 1. Statistics of Data Collection, MIR Phasing, and Crystallographic Refinement**

| Crystal | Native Form I | TMLA Derivative | $K_2PtCl_6$ Derivative | $KAuCl_4$ Derivative | Native Form II |
|---|---|---|---|---|---|
| Constructs | VPS36 (170-386) | | | | VPS36 (149-386) |
| | VPS22 (26-258) | | | | VPS22 (1-258) |
| | VPS25 (1-176) | | | | VPS25 (1-102) |
| Space group, unit cell | $P2_1$, a = 70.2, b = 89.2, c = 91.4, β = 101.5 | | | | $P3_212$, a, b = 81.5, c = 226.2 |
| Heavy atom soaking condition | | 10 mM, 1 day | 1 mM, 2hr | 2 mM, 1 day | |
| X-ray source | SER-CAT 22-ID | $CuK_\alpha$ | $CuK_\alpha$ | $CuK_\alpha$ | SER-CAT 22-ID |
| Wavelength (Å) | 1.0000 | 1.5418 | 1.5418 | 1.5418 | 1.0000 |
| Resolution (Å) (last shell) | 2.6 (2.69–2.60) | 3.6 (3.73–3.60) | 3.1 (3.21–3.10) | 3.2 (3.31–3.20) | 2.9 (3.0–2.9) |
| No. of unique reflections | 30680 | 11712 | 19725 | 17604 | 19408 |
| I/σ (last shell) | 33.0 (3.1) | 16.1 (5.0) | 28.8 (4.5) | 23.8 (4.2) | 41.3 (3.3) |
| $R_{sym}$[a] (%) | 4.9 (30.2) | 10.6 (33.1) | 7.1 (41.3) | 8.4 (43.3) | 4.7 (42.9) |
| Data completeness (%) | 91.4 (61.1) | 94.7 (96.5) | 99.9 (100.0) | 99.8 (99.5) | 99.6 (99.5) |
| Phasing and refinement | | | | | |
| Mean FOM (50–3.6 Å) | | | 0.54 (SOLVE) | | MR |
| Overall FOM (50–3.6 Å) | | | 0.75 (RESOLVE) | | |
| R factor[b] (%) | 23.8 | | | | 23.2 |
| Free R factor[c] (%) | 29.4 | | | | 31.7 |
| Rms bond length (Å) | 0.013 | | | | 0.010 |
| Rms bond angle (°) | 1.463 | | | | 1.275 |
| Average B value (Å$^2$)[d] | 78.7 | | | | 89.8 |
| | HD (V22 34–76, V36 172–225) 124.7 | | | | HD 101.6 |
| | core (V22 77–252, V36 226–385) 61.2 | | | | core 79.1 |
| | VPS25 84.7 | | | | VPS25 100.8 |

The values in parentheses relate to highest resolution shells.
[a] $R_{sym} = \Sigma_h \Sigma_i |I_i(h) - \langle I \rangle| / \Sigma_h \Sigma_i I_i(h)$, where $I$ is the observed intensity and $\langle I \rangle$ is the average intensity of multiple observations of symmetry-related reflections.
[b] $R = \Sigma||F_o| - k|F_c|| / \Sigma|F_o|$, where $F_o$ and $F_c$ are observed and calculated structure factor amplitudes, respectively.
[c] $R_{free}$ is calculated for a randomly chosen 5% of reflections; the R factor is calculated for the remaining 95% of reflections used for structure refinement.
[d] Average B value of all atoms in an asymmetric unit.

subunits project from the ordered core of the complex. The N terminus of Vps22 contains a long helical region of unknown function. A ~100 residue predicted helical region of unknown structure and function connects the Vps36 GLUE domain to the core. Structural information has been rapidly accumulating for most of the ESCRT components, allowing, for example, the reconstruction of a hydrodynamic model of intact ESCRT-I from the crystal structures of the constituent fragments (Kostelansky et al., 2007). The main obstacle to a similar model for the intact ESCRT-II has been the lack of information on the ~100 residue helical connector in Vps36 and the N-terminal helical region of Vps22. Here, we report the structures of two human ESCRT-II constructs that include these regions. These two regions fold into a compact helical bundle, except for the N-terminal ~25 amino acids of Vps22, which we find has a role in membrane targeting. On the basis of this and previous structures (Alam et al., 2006; Hirano et al., 2006) and hydrodynamic measurements, we develop a unified model for the structure of intact ESCRT-II. We extend the observation on the N terminus of Vps22 to develop a model of dual membrane targeting by this region and the GLUE domain.

## RESULTS

### Crystallographic Analysis of Human ESCRT-II

The 2.6 Å crystal structure of the human ESCRT-II complex lacking the GLUE domain was solved by multiple isomorphous replacement (form I: Table 1; Figures 1A–1D). The complex contains two molecules of VPS25, one molecule of VPS22, and one copy of VPS36. It has a trilobal shape similar to that of yeast ESCRT-II (Hierro et al., 2004; Teo et al., 2004; Figure S1, see the Supplemental Data available with this article online). Two of the lobes consist of VPS25 subunits, and the third consists of VPS36 and VPS22 (Figures 1B and 1C). The VPS22 and VPS36 subunits form a roughly parallel side-to-side arrangement. There is an extensive interface between VPS22 and VPS36, with a buried surface area of 2225 Å$^2$. The first four helices of VPS22 and the first three helices VPS36 in this structure form a novel helical domain (HD) (Figure 2A). This conserved helical domain was absent in the structure of yeast ESCRT-II because the sequences corresponding to the first three helices of Vps36 were absent from the crystallized portion of yeast ESCRT-II (Figure 1A; Hierro et al., 2004; Teo et al., 2004). The HD is one of the most mobile

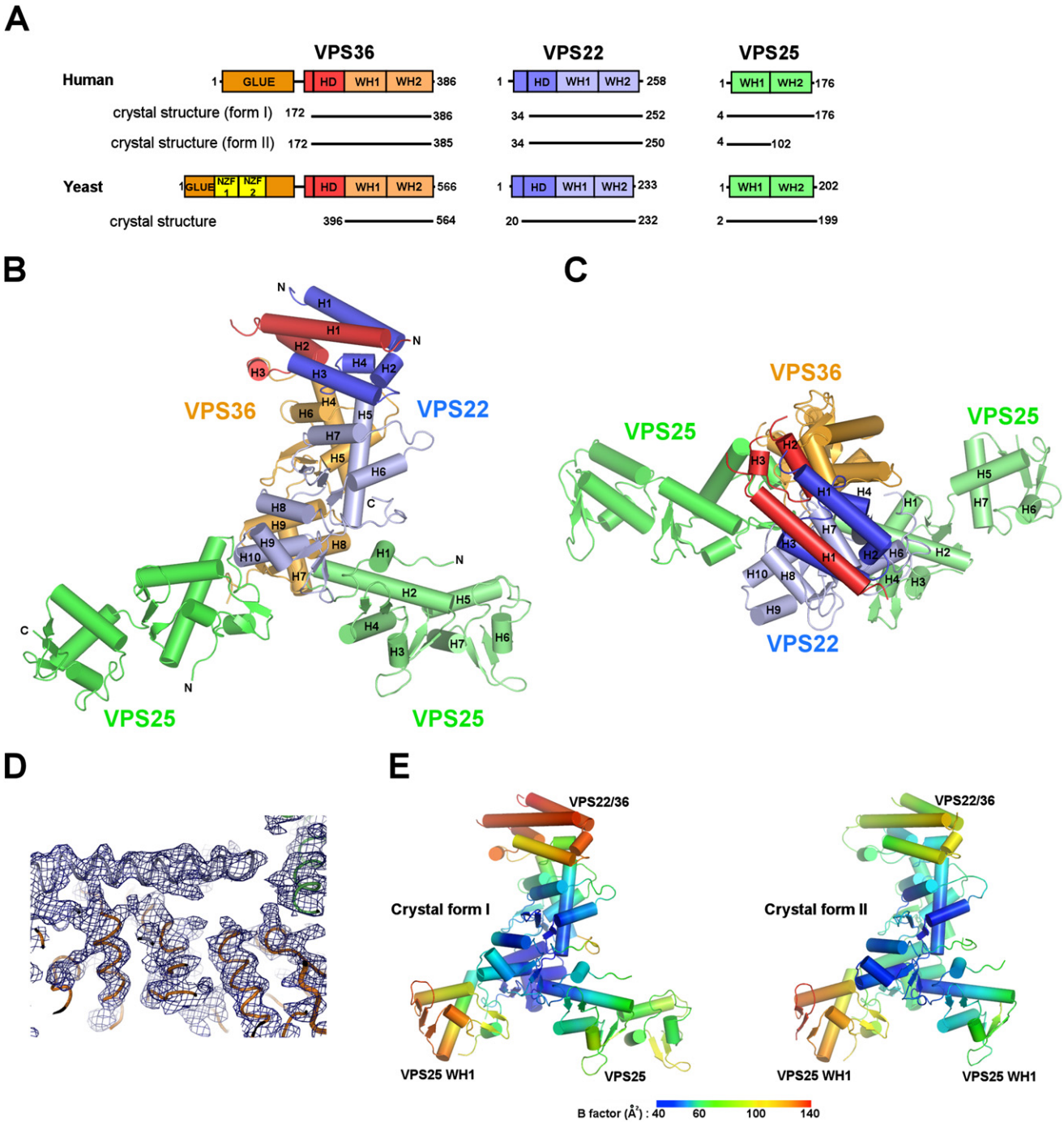


**Figure 1. Structure of Human ESCRT-II Complex**

(A) Schematic of ordered regions visualized in human (this study) and yeast ESCRT-II (Hierro et al., 2004; Teo et al., 2004) complexes, with a comparison to the domain structures of intact human and yeast ESCRT-II complexes.

(B) Overall structure of the complex. The WH2 domain of one of the VPS25 subunits was poorly visible in the electron density map and it was not included in the structure refinement. The missing VPS25-WH2 was modeled in the figure using the structure of the other subunit.

(C) A top view of the complex showing a relatively flat "profile" of the complex.

(D) Electron density from a solvent-flattened MIR map contoured at 1.0 σ in the vicinity of VPS22-VPS36 portion of the core. The final refined structure was shown in a tube model.

(E) Crystal structures in forms I and II are shown colored by B factor to show regions of high (red) and low (blue) mobility.

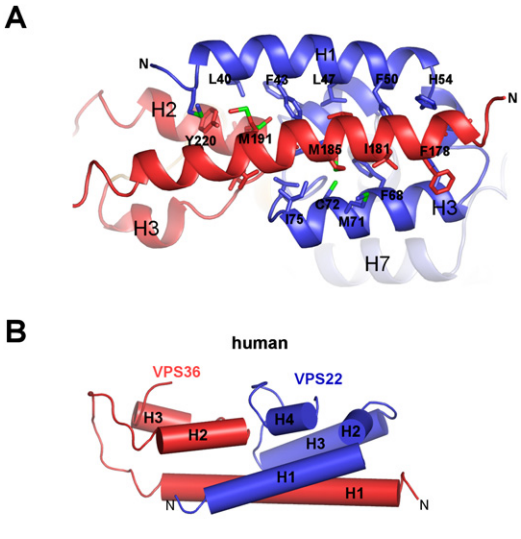


**Figure 2. The Helical Domain of ESCRT-II**

(A) N-terminal helical domain (HD) of VPS22 and VPS36.

(B) Comparison of human and yeast ESCRT-II in the HD region. The newly observed N-terminal helical domain formed by human VPS22 and VPS36 is shown at left, as compared to the isolated Vps22 fragment of this domain seen in the yeast structure at right.

regions of the human ESCRT-II crystal structure. Indeed, the HD helices of VPS22 and VPS36 subunits have sausage-like electron density. The presence of a few protruding bulky side chains allowed for sequence assignment. The linker connecting helices H1 and H2 (residues 202–211) in the VPS36 subunit was not visible in the structure. The overall B value of the ESCRT-II core complex is 78.7 Å$^2$. However, the average B value of the HD is 124.7, compared to an average B value of 61.2 Å$^2$ for the remainder of the structure (Figure 1E, left hand panel). This suggested to us that the HD was either loosely packed in the crystal lattice or that it had intrinsically high mobility.

VPS22, VPS25 and VPS36 each contain two repeats of a winged helix (WH) domain with an H1/β1/H2/H3/β2/β3 topology. The N-terminal WH domain (WH1) packs against the C-terminal WH domain (WH2) in a head-to-tail manner. All of the WH domains in the ESCRT-II complex superimpose on each other with an rmsd of less than 2 Å, although there is no recognizable sequence similarity between the subunits.

The N-terminal domain of one VPS25 subunit contacts the C-terminal domain of VPS22, and the other VPS25 subunit contacts both VPS36 and VPS22. The VPS25 subunit buries 762 Å$^2$ (63 Å$^2$ for VPS22) of surface area upon binding to VPS36, and the other VPS25 subunit buries 1149 Å$^2$ of surface area upon binding to VPS22 and VPS36. The WH2 domain of the VPS36-proximal VPS25 subunit, which packs in the crystal lattice along the c-axis, appears to be completely disordered and could not be visualized in an electron density map. This suggested to us that VPS25 has intrinsic flexibility between its two WH domains.

The N-terminal 25 residues of VPS22 contain 8 basic charged residues and are predicted to form an α helix (Figure S2). We refer to this predicted helix as VPS22-H0. The linker between the GLUE domain and the C-terminal core of VPS36 (residues 140–169) also contains a predicted α helix, which we refer to as VPS36-H0 (Figure 2D). In an effort to reveal the structure of these N-terminal regions of VPS22 and VPS36 and to obtain more detailed information on the HD, we determined the 2.9 Å crystal structure (form II, Table 1) of a second construct (construct a, Figure 3C). The flexible WH2 domain of VPS25 was deleted in the second construct in an attempt to generate more ordered crystals. The structures of forms I and II are almost identical with an rmsd of 1.25 Å$^2$. Form II manifested better electron density in the HD. It was possible to visualize the linker between H1 and H2 of VPS36. The improved density also allowed us to confirm the assignment of amino acids in the HD. The VPS22-H0, VPS36-H0, and adjoining residues were disordered. A solvent channel takes the space that is presumably occupied by the disordered N-terminal region in the crystal. The average B value of HD is 101.6 Å$^2$, which is higher than the value of 79.1 Å$^2$ for the remainder of the structure, although lower than the HD in form I (Figure 1E). The finding that the HD region has such high B factors in two different crystal forms leads us to conclude that this domain is inherently dynamic.

## Solution Conformation of the Complete ESCRT-II Complex

To investigate the conformation of the full-length ESCRT-II complex in solution, we measured the Stokes radii $R_H$ of various ESCRT-II constructs. The Stokes radii of the constructs were obtained using size exclusion chromatography (SEC) calibrated with standards of known $R_H$ (Figure 3A). To gain insight on the overall shape of full-length ESCRT-II, we positioned the GLUE domain structure (Alam et al., 2006; Hirano et al., 2006) based on the $R_H$ values from SEC experiments (Figures 3A and 3B). The position of the GLUE domain was adjusted until the calculated $R_H$ agreed with the experimental values to within 0.1 nm. Conformations involving an extended linker between the crystallized core and the GLUE domain can be ruled out because these predict $R_H$ values substantially higher than are actually observed (Figure S3). On the other hand, conformations in which the GLUE domain is packed against the WH domains lead to predicted $R_H$ values that are lower than the experimental value. Based on this exercise, we concluded that the GLUE domain is probably packed against the HD domain of the crystallized ESCRT-II core and that human ESCRT-II is in a compact, closed conformation in solution (Figure 3B).

## Interactions between Human ESCRT-I and ESCRT-II

The yeast ESCRT-I interacts with ESCRT-II via the C-terminal domain (CTD) of Vps28 (Kostelansky et al., 2006; Teo et al., 2006) and the NZF1 domain of Vps36 (Gill et al., 2007; Teo et al., 2006). However, human ESCRT-II contains no NZF domains. Evidence for binding between human ESCRT-I and II comes from yeast two-hybrid analyses of pairwise interactions

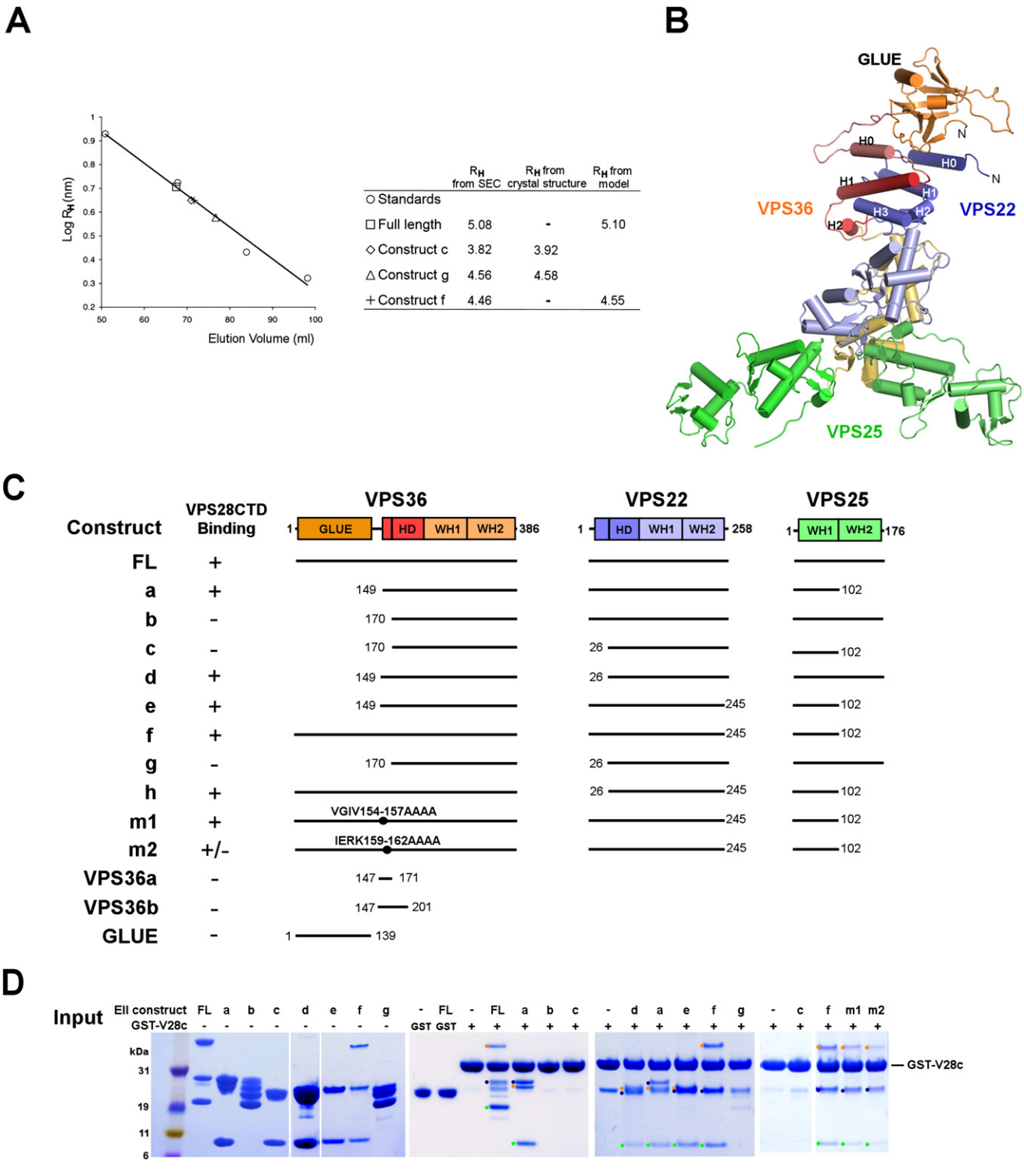


| | $R_H$ from SEC | $R_H$ from crystal structure | $R_H$ from model |
|---|---|---|---|
| ○ Standards | | | |
| □ Full length | 5.08 | - | 5.10 |
| ◇ Construct c | 3.82 | 3.92 | |
| △ Construct g | 4.56 | 4.58 | |
| + Construct f | 4.46 | - | 4.55 |

**Figure 3. Solution Structure and ESCRT-I Interactions of ESCRT-II**

(A) Analysis of recombinant ESCRT-II complex on a Superdex 200 (16/60) column monitored by absorption at 280 nm. Comparison of the intact ESCRT-I Stokes radius $R_H$ derived from size exclusion data. The calculated $R_H$ values from crystal structures of the ESCRT-II constructs correspond precisely to the value expected from fitting to gel filtration standards. The standards are shown in open circles (BioRad) and consist of bovine thyroglobulin (670 kDa, $R_H$ = 8.5 nm), bovine γ-globulin (158 kDa, $R_H$ = 5.3 nm), chicken ovalbumin (44 kDa, $R_H$ = 2.7 nm), and horse myoglobin (17 kDa, $R_H$ = 2.1 nm).

(B) Solution conformation of intact ESCRT-II derived by fitting structural coordinates to hydrodynamic data from the four constructs shown in (A) using Hydropro (Garcia de la Torre et al., 2000).

(C) Constructs used in this study.

between subunits of ESCRT-I and II (Langelier et al., 2006). However, isolated ESCRT subunits expressed for two-hybrid studies contain extensive unpartnered hydrophobic regions. Under physiological conditions, these would be buried within the larger complex. Given the presence of significant conserved sequences on the surface of the Vps28 CTD (Gill et al., 2007; Pineda-Molina et al., 2006) and 36% sequence identity between the yeast and human CTD sequences, we speculated that this domain might have a conserved role in binding to ESCRT-II. Thus, we sought to revisit the interaction between human ESCRT-I and II using the purified, stable, independently folded VPS28 CTD and various forms of the purified, fully assembled ESCRT-II complex in direct binding assays (Figures 3C and 3D).

The full-length ESCRT-II construct binds to VPS28-CTD, but not to the GST control (Figure 3D). Constructs in which the GLUE domain, the VPS25 WH2 domain, and VPS22-H0 (constructs a, d, e, and f, Figure 3D) were deleted, respectively, also bind to the VPS28-CTD. However the constructs lacking residues 149–169, which encompass VPS36-H0, did not interact with VPS28-CTD, suggesting that the VPS36-H0 and/or adjacent residues are required for binding to the VPS28-CTD. The role of this region of VPS36 is consistent with the two-hybrid analysis (Langelier et al., 2006). In order to pinpoint this site, two blocks of conserved residues were mutated to polyalanine. A quadruple mutant within VPS36-H0 (construct m2), IERK(159-162)AAAA, showed substantially reduced binding as compared to wild-type and to another, mutant (construct m1, Figure 3C). GST-tagged constructs of short regions of VPS36 (residues 147–171 and residues 147–201) were made to test if these isolated regions were sufficient for binding. These constructs did not pull down VPS28-CTD (Figures 3C and 3D), nor did the isolated GLUE domain (Figure 3C; data not shown). Thus, VPS36-H0 is necessary but not sufficient for interaction with the VPS28-CTD. We sought to characterize the conformation of the VPS28-CTD-ESCRT-II complex in solution. The mixture of these two normally soluble proteins resulted in their precipitation. The simplest interpretation is that the binding of the VPS28-CTD and ESCRT-II leads to a conformational change in one or both partners.

## Determinants for Membrane Targeting of Human ESCRT-II

To investigate the lipid specificity and membrane binding sites in human ESCRT-II, we tested binding of various ESCRT-II constructs to lipid vesicles of various compositions (Figure 4). For expediency, we used a pseudo-intact ESCRT-II (construct f, Figure 3C) lacking the VPS25-WH2 as the baseline for comparison. This construct bound to vesicles as well as, or better than, the intact complex (Figure S4), and we found that it was more stable and could be purified with several-fold higher yields than the intact complex. The following deletion constructs were made in the context of this pseudo-intact complex: a deletion of GLUE domain (construct e), a deletion of the basic N-terminal 24 residues (Δ1–24) of VPS22 (construct h), and a double deletion of both the GLUE and VPS22-H0 (construct c). The purified pseudo-intact ESCRT-II showed strong binding to liposomes made of synthetic lipids composed of phosphatidylcholine (PC), phosphatidylethanolamine (PE), and phosphoinositides (PIPs) (Figures 4D–4K) and bound weakly to PC:PE and PC:PE:phosphatidylinositol (PI) liposomes (Figures 4B, 4C, and 4K). Deletion of the VPS22-H0 (construct h) significantly decreased the membrane binding to all PIPs tested. However, deletion of VPS22-H0 had no apparent effect on binding to PC:PE liposomes (Figures 4B and 4K). The GLUE domain deletion lost binding to PC:PE and PC:PE:PI (Figures 4B, 4C, and 4K). Deletion of both GLUE and Δ1–24 of VPS22 (construct c) essentially abolished binding to all compositions tested (Figures 4B–4K). From these data, we draw the following conclusions. Human ESCRT-II binds strongly but relatively promiscuously to PIPs and binds weakly to uncharged lipids. Both the GLUE domain and VPS22-H0 are required for full membrane binding.

## A Functional Role for Vps22-H0

The Vps22-H0 is conserved from yeast to humans, with 30% sequence identity between these two species in this region (Figure S2). To determine if the Vps22-H0 was important for the cargo sorting function of ESCRT-II in vivo, the localization of the ESCRT substrate Cps1 was assayed in yeast expressing wild-type and mutant alleles of *vps22*. Yeast Vps22 contains 9 basic charged residues in the N-terminal 50 residues. To test the contribution of the N-terminal region of Vps22 on cargo-sorting function in vivo, we constructed an N-terminal 30 residue deletion mutant, $Vps22^{\Delta 1\text{-}30}$ (Figure S2). As expected (Babst et al., 2002), *vps22Δ* manifests GFP-Cps1 mislocalized to a prominent class E compartment and is absent from the vacuolar lumen (Figure 5B). The wild-type phenotype is completely rescued by a plasmid bearing wild-type *VPS22* (Figure 5E). Expression of $VPS22^{\Delta 1\text{-}30}$ results in some vacuolar GFP-Cps1 localization (Figure 5F) but most of the cargo is retained on the limiting membrane, consistent with a weak class E phenotype. This indicates that the Vps22-H0 is important for the cargo-sorting function of ESCRT-II.

We next sought to determine if Vps22-H0 cooperated with the Vps36-GLUE domain in function. The yeast Vps36 GLUE domain PI(3)P binding pocket double-mutant $VPS36^{R89A/R261A}$ has a strong class E phenotype (Teo et al., 2006). We found that the single GLUE domain mutants $VPS36^{R89A}$ and $VPS36^{R261A}$ expressed in a *vps36Δ* background had near normal and normal function, respectively (Figures 5H and 5I). However, when either of these mutants is coexpressed with $VPS22^{\Delta 1\text{-}30}$ in a *vps22Δ vps36Δ* background, a strong class E phenotype is observed (Figures 5K and 5L). The loss of function is much stronger than for any of the individual mutants, consistent with the concept that the Vps22-H0 and the Vps36-GLUE domain cooperate in the sorting function of ESCRT-II.

In order to determine if the defects in sorting were due to changes in membrane targeting, the localization of wild-type and mutant Vps22-GFP constructs was evaluated (Figures 5M–5S). ESCRT components are diffusely localized in wild-type yeast because of the rapid recycling of endosomal ESCRTs to the cytosol as part of their normal function. However, in *vps4Δ* strains, the

(D) GST-pull down experiment showing a direct interaction between VPS28-CTD and the various ESCRT-II constructs. The ESCRT-II constructs used for the assay are shown in lanes 2–8 for reference. The absence of binding of full-length ESCRT-II to GST-bound beads is shown in lanes 9 and 10 as a control. Bands corresponding to subunits of complexes that are positive for VPS28-CTD binding are highlighted with dots colored as in (B).

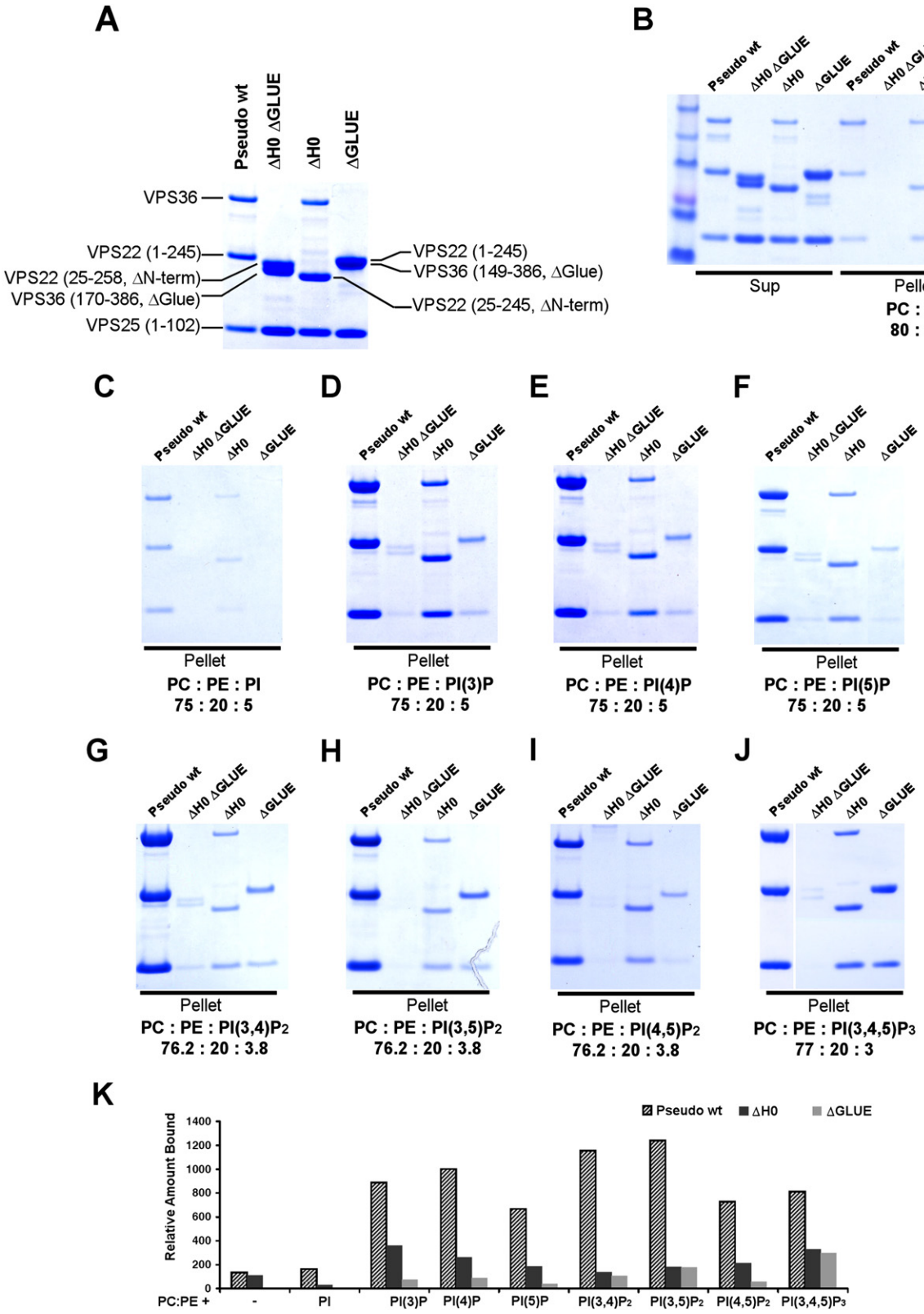


**Figure 4. Liposome Binding of ESCRT-II Complex**

Purified constructs of the ESCRT-II complex were mixed with liposomes.

(A) The ESCRT-II constructs used for liposome binding assay are shown for reference. All constructs used for the binding assay lack the VPS25-WH2 for expedience. However, the binding of this construct and full-length ESCRT-II are essentially identical (Figure S3).

dissociation of ESCRT components from endosomal compartments is inhibited, allowing their endosomal localization to be monitored. Consistent with previous results (Babst et al., 2002), Vps22-GFP was diffusely distributed in a *vps22Δ* background (Figure 5M) but found in large punctate structures in a *vps4Δ vps22Δ vps36Δ* strain (Figure 5N). The single GLUE domain mutants $VPS36^{R89A}$ and $VPS36^{R261A}$ manifested, respectively, complete and predominant punctate localization of Vps22-GFP in the *vps4Δ vps22Δ vps36Δ* strain (Figures 5P and 5Q). Therefore, these mutations did not substantially impair ESCRT-II targeting. The $VPS22^{\Delta 1\text{-}30}$*-GFP* allele manifested mostly punctate localization, with a small increase in diffuse localization compared to wild-type *VPS22* (Figure 5O). The $VPS22^{\Delta 1\text{-}30}$*-GFP* allele in combination with either $VPS36^{R89A}$ or $VPS36^{R261A}$, however, showed a completely diffuse localization pattern (Figures 5R and S5). Thus, these defects in the Vps22-H0 and GLUE domain abolish endosomal localization of ESCRT-II only in combination.

## DISCUSSION

A major goal of structural analysis is to obtain a holistic picture of molecular assemblies. This is typically accomplished by integrating high-resolution X-ray and NMR structures of smaller fragments with lower resolution data on the intact complex using electron microscopy or solution-state techniques. In the case of ESCRT-II, atomic structures have been available for the WH domain core (Hierro et al., 2004; Teo et al., 2004), the NZF1 domain (Gill et al., 2007), and the GLUE domain of the yeast complex (Teo et al., 2006) and the GLUE domain of the human complex (Alam et al., 2006; Hirano et al., 2006). One essential component was lacking to model the complete ESCRT-II structure: the structure of the predicted helical regions in the Vps22 N terminus and in Vps36 between the GLUE and WH domains. We have now found that the most N-terminal predicted helix of the core of each subunit (H0) is flexibly attached to the core assembly. We have been able to assign functions to each of these two regions. The VPS22-H0 participates in membrane binding, while the VPS36-H0 interacts with ESCRT-I. The most significant finding from the crystallographic analysis is that ESCRT-II contains a helical domain composed of portions of both the VPS22 and VPS36 subunits. As described below, this domain appears to serve as a structural platform for the GLUE domain.

While ESCRT-II is too small to yield a cryo-EM reconstruction, we have been able to use hydrodynamic analysis (Garcia de la Torre et al., 2000; Kostelansky et al., 2007) together with the ESCRT-II core structure and the previously determined structure of the GLUE domain (Alam et al., 2006; Hirano et al., 2006) to model the conformation of the complete human complex in solution. This analysis shows unambiguously that human ESCRT-II has a compact conformation in solution. This is in sharp contrast to the ESCRT-I complex, where the functional domains extend away from the core on freely flexing linkers (Kostelansky et al., 2007). The constraints imposed by known crystal structures and by experimental hydrodynamic data indicate that the GLUE domain must directly contact the helical domain. Thus, one function of the helical domain appears to be to scaffold the GLUE domain in the closed conformation of ESCRT-II.

Current models of ESCRT function invoke either the sequential or cooperative assembly of multiple ESCRT complexes on the endosomal membrane (Hurley, 2008; Nickerson et al., 2007; Saksena et al., 2007; Williams and Urbe, 2007). The yeast ESCRT-I and -II complexes assemble together through a required interaction between the ESCRT-I Vps28-CTD and the ESCRT-II Vps36 NZF1 domain (Gill et al., 2007), although the existence of additional interactions has not been ruled out. Indeed, we find that the yeast ESCRT-I/II supercomplex is compact in solution (M.S. Kostelansky and J.H.H., unpublished data), consistent with the presence of more than one interaction site. Human ESCRT-II lacks an NZF domain, and the available evidence that it interacts directly with human ESCRT-I has been limited to two-hybrid studies of isolated subunits (Langelier et al., 2006). Here, we find that human ESCRT-II interacts robustly with the human VPS28-CTD. A motif within the ESCRT-II VPS36-H0 is necessary but not sufficient for this interaction. This motif is conserved in yeast Vps36, consistent with the possibility that the yeast ESCRT-I/II interaction involves more than one point of contact. The observation that the motif is necessary but not sufficient for the interaction suggests to us that ESCRT-I recognition by ESCRT-II involves an extended epitope.

Based on the highly dynamic nature of the ESCRT-II HD region and the observation of a dramatic solubility change upon mixing ESCRT-II and the ESCRT-I VPS28-CTD, we speculate that formation of the ESCRT I/II supercomplex entails a large conformational change. A similar solubility change was observed when yeast ESCRT-II or its Vps25 subunit was mixed with the yeast ESCRT-III subunit Vps20 (Teo et al., 2004). It will be interesting to assess whether there are widespread conformational changes when ESCRTs assemble with one another and with membranes. Such changes could have important implications for the membrane-remodeling interactions that are catalyzed by the ESCRT system.

The mechanism of membrane targeting by ESCRT-II has attracted considerable attention. ESCRT-II is functionally activated by ESCRT-I. However, ESCRT-I is not required for the recruitment of ESCRT-II, since the loss of ESCRT-I can be rescued by the overexpression of ESCRT-II subunits (Babst et al., 2002). Yeast ESCRT-II binds with moderate-to-high affinity to PIP-containing liposomes in the absence of ESCRT-I (Kostelansky et al., 2007; Teo et al., 2004, 2006). The principal site for PIP binding was first localized to the GLUE domain in studies of human ESCRT-II by Stenmark and colleagues (Slagsvold et al., 2005). This study showed that the human ESCRT-II GLUE domain bound in vitro to immobilized $PI(3,4,5)P_3$ in a dot-blot format and, to a lesser extent, to $PI(3,4)P_2$ and $PI(3,5)P_2$ (Slagsvold et al., 2005). $PI(3,4,5)P_3$ is typically present at the plasma membrane of cells stimulated by hormones such as insulin and PDGF, but is not characteristic of endosomal membranes. The GLUE

(B) Binding to PC:PE liposomes. Molecular weight markers are shown in lane 1. Unbound samples in supernatants were shown in lanes 2–5 for reference.
(C–J) Liposome binding results with different lipid compositions. Variable amounts of PI and PIPs were mixed to the PE: PC mixture to examine the specificity. The mole fractions of PIPs were chosen to maintain a constant charge density on the membrane.
(K) The relative amounts of proteins in the pellets were shown in bars. The construct double deletion construct (c), which shows negligible binding to all liposomes tested, is not shown in bar graphs.

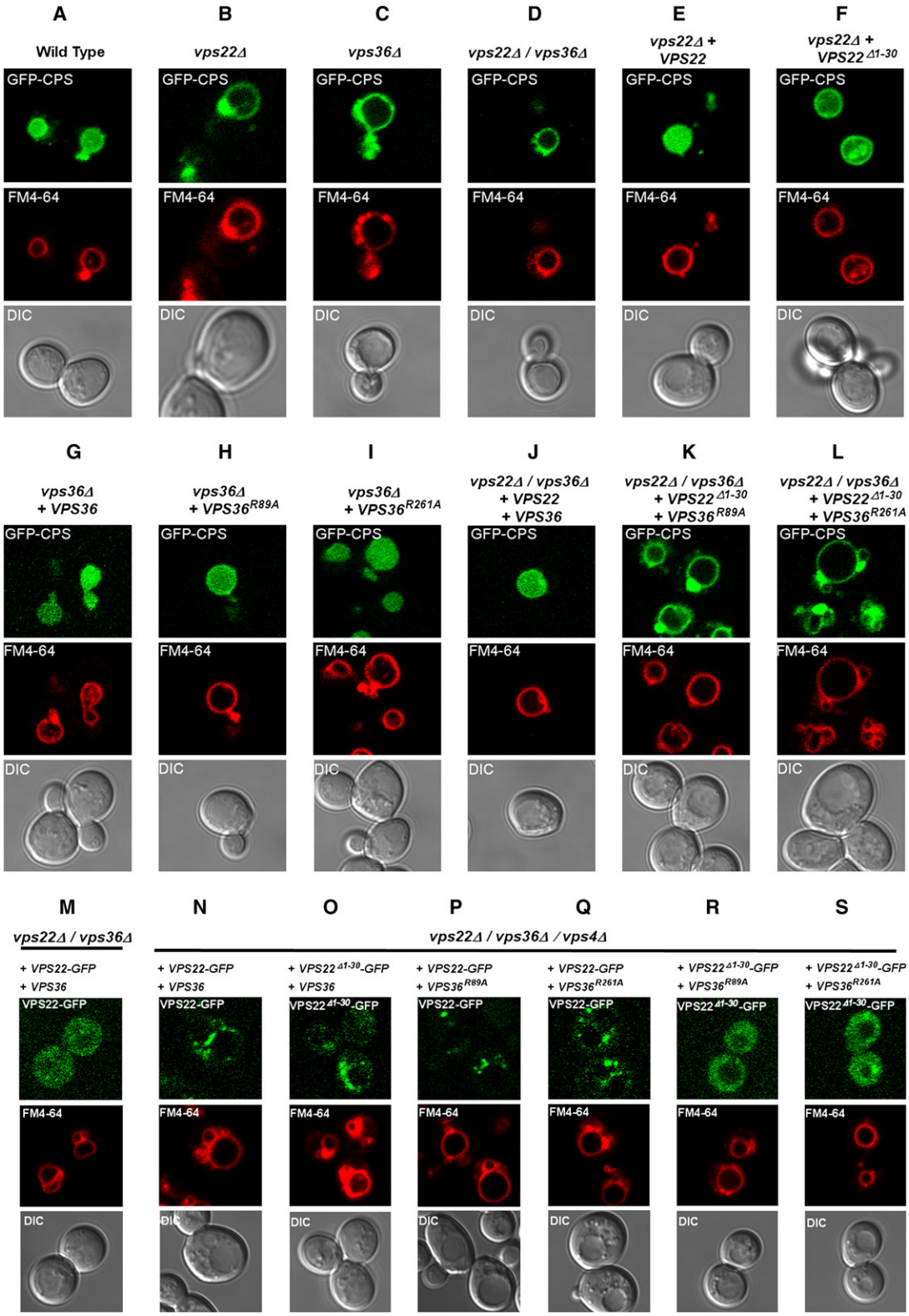


**Figure 5. Cargo Sorting and Localization of Vps22 and Vps36 Mutants**

(A–L) The uppermost panel of each column shows the sorting of the GFP-Cps1 construct (green) in various strains, as indicated at the top of each column. (M–S) The localization of the designated ESCRT-II constructs in the indicated strains, as monitored by Vps22-GFP. The middle panels show the limiting membrane of the vacuole as labeled by FM4-64 (red), and the lower panels show the DIC image. Results presented here are characteristic of observations of >100 cells for each strain shown.

domain of yeast ESCRT-II, in contrast, bound preferentially to PI(3)P when presented in liposomes, and the isolated yeast GLUE domain targets to endosomes when expressed in cultured human cells (Teo et al., 2006). Here, we deduce, based on comparison of the intact and GLUE-domain deleted ESCRT-II complexes, that the human ESCRT-II GLUE domain binds to a variety of phosphoinositides. Deletion of the GLUE domain sharply reduces binding to the endosomal lipids PI(3)P and PI(3,5)$P_2$ but more modestly reduces binding to PI(3,4,5)$P_3$. Deleting Vps22-H0 has a modest effect on binding to PI(3)P and most other PIPs compared to the GLUE domain deletion. However, the Vps22-H0 deletion reduces binding to PI(3,5)$P_2$ and PI(3,4,5)$P_3$ by about the same extent as the GLUE domain deletion. We infer there is a strong electrostatic interaction between Vps22-H0 and the polyanionic PI(3,5)$P_2$ and PI(3,4,5)$P_3$. The ability of human ESCRT-II to bind to PI(3)P and PI(3,5)$P_2$ is consistent with the endosomal function of ESCRT-II. The binding to PI(3,4,5)$P_3$ and other nonendosomal PIPs is consistent with the previous report of a GLUE-PI(3,4,5) $P_3$ interaction (Slagsvold et al., 2005) but hard to rationalize in terms of the endosomal role of ESCRT-II. The GLUE domain of *Drosophila* ESCRT-II, which more closely resembles human as opposed to yeast ESCRT-II, binds to bicoid mRNA (Irion and St Johnston, 2007). Thus, the propensity of human ESCRT-II to bind highly acidic lipids may reflect this or other nonendosomal functions (Slagsvold et al., 2006) that involve binding to various highly acidic ligands.

The observation that both the Vps36 GLUE domain and the Vps22 H0 contribute to lipid binding in vitro suggested to us that a combinatorial mechanism evolved to drive high-affinity membrane targeting of ESCRT-II (Figure 6). Multivalent membrane targeting is widely used in the ESCRT system and other trafficking pathways for signal integration and coincidence detection. Given that ESCRT-I is involved in the functional activation of ESCRT-II, it is intriguing that ESCRT-I binds to a region of ESCRT-II very close to the locus of membrane binding and that this interaction appears to trigger a structural change. In conclusion, we have derived here a structural and conceptual framework for a more precise mechanistic understanding of the interplay between ESCRT-I and membrane binding by ESCRT-II. More importantly, the organization of ESCRT-II deduced here, together with similar models for the overall structures of the Vps27-Hse1 (Prag et al., 2007) and ESCRT-I (Kostelansky et al., 2007) complexes, will underpin higher order structural studies of the ESCRT system.

## EXPERIMENTAL PROCEDURES

### Protein Expression and Purification

Full-length genes for human VPS22, VPS25, and VPS36 were synthesized by PCR-based gene synthesis. Oligonucleotides were designed by the program DNAWorks (Hoover and Lubkowski, 2002). The nucleotide sequences of the genes were optimized for expression in *E. coli*, and restriction enzyme recognition sequences in the multiple cloning sites of pST39 vector were removed from the genes for efficient cloning of multiple genes into the vector. VPS22 was tagged with an N-terminal hexahistidine and a TEV protease cleavage site. The plasmid was transformed into *E. coli* strain BL21(DE3) Star and expressed overnight at 30°C. Cells were resuspended in buffer (2X PBS plus 20 mM imidazole) and lysed by sonication. The ESCRT-II complex was isolated using $Ni^{2+}$ affinity chromatography. The eluate was concentrated and the histidine tag was removed with TEV protease. The ESCRT-II complex was further purified by a Superdex S200 size exclusion chromatography.

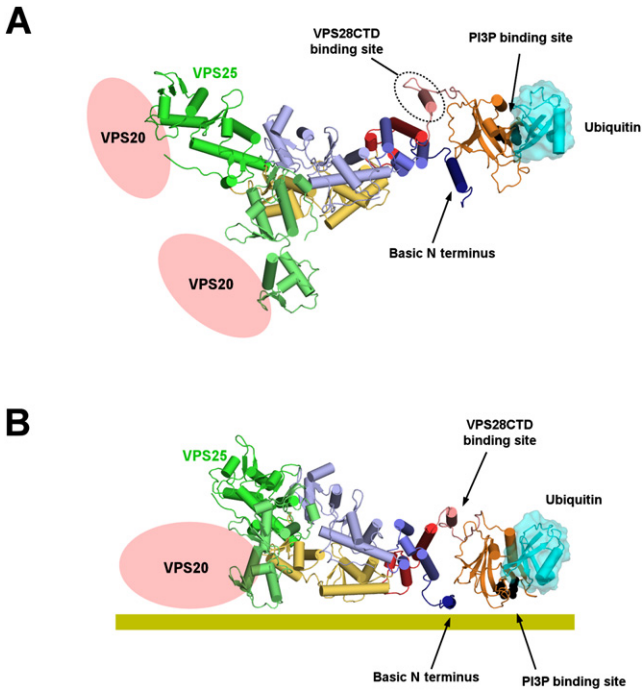


**Figure 6. Combinatorial Membrane Targeting of ESCRT-II**

(A) Overall schematic representation of full-length ESCRT-II structure showing the binding site for VPS28-CTD and the VPS22-H0 examined in this study, and the previously described binding sites for PI(3)P (Teo et al., 2006), ubiquitin (Alam et al., 2006; Hirano et al., 2006), and VPS20 (Langelier et al., 2006).

(B) Model for combinatorial targeting by specific and nonspecific interactions with membrane (represented by the solid horizontal bar) lipids.

The fractions containing the complex were concentrated in buffer 10 mM Tris-HCl (pH 8.0), 100 mM NaCl.

### Crystallization

Form I crystals of construct g (Figure 3C) were grown by vapor-diffusion methods at 25°C over a reservoir of 100 mM Na-Acetate (pH 4.5), 5% PEG 4000, 15% glycerol for 1 week. Crystals were cryoprotected in reservoir solution supplemented with 20% (v/v) glycerol and flash frozen under $N_2$ gas at 95 K. Heavy atom derivative crystals were prepared by cocrystallization or by soaking crystals in heavy atom solutions. Form II crystals of construct a (Figure 3C) were obtained in 100 mM Tris-HCl (pH 8.5), 40% PEG300 using a microseeding technique.

### Crystallographic Analysis

Native data for the form I crystal VPS36 GLUE domain and VPS22 H0 truncation (construct g, Figure 3) were collected to 2.6 Å resolution from a single frozen crystal with an MAR CCD detector at beamline 22-ID, APS. The data sets were anisotropic with weak diffraction along c extending only to 2.9 Å resolution. All data were processed and scaled using HKL2000 (HKL Research). Heavy atom derivative data sets were collected with an R-AXIS IV image-plate system attached to a Rigaku rotating-anode generator providing Cu $K_\alpha$ radiation. MIR phasing was carried out using the program SOLVE (Terwilliger and Berendzen, 1999) at 3.6 Å resolution (Table 1), and the phases were further improved by RESOLVE (Terwilliger, 2000). The initial model was built manually into the density-modified map using the programs O (Jones et al., 1991) and Coot (Emsley and Cowtan, 2004). Tracing of the backbones was facilitated by comparing the homologous structure of yeast ESCRT-II complex; then the density map was improved using model phase combination and the resolution was extended to 2.6 Å resolution. The refinement was carried out using CNS (Brunger et al., 1998) and Refmac (CCP4, 1994). The final model for form I consisted of residues 172–385 from VPS36, residues 34–252 from VPS22, and

residues 4–176 and 5–101 from VPS25. There are 97.2% of the residues in the most favored and additional allowed regions of the Ramachandran plot. Seven residues have conformations in disallowed regions, and all of these are located in regions of high mobility at the extreme termini of chains, in the helical domain, or in the flexible VPS25 WH2 domain. The structure of the form II crystal (construct a, Figure 3) was determined by molecular replacement with the program MOLREP using the form I structure as a starting model. Residues 149–169 from VPS36 and residues 1–25 from VPS22 are present in construct a, but could not be visualized in electron density and are presumed to be disordered. All structural figures were prepared using the program PyMOL (W. Delano, http://pymol.sourceforge.net/).

### Hydrodynamic Modeling

Residues in the N and C termini of the subunits (residues 1–3 in VPS25, 27–33 and 253–258 in VPS22) that were present in the crystallized construct of form I but missing in the electron density were modeled as random coils, and the random coil conformation was adjusted iteratively with interactive graphics until the calculated and experimental $R_H$ values were in agreement within < 0.1 nm (Figure 3A). Essentially the same procedure was used to place VPS22-H0 and VPS36-H0, which were modeled as helices on the basis of secondary structure prediction, using the crystal structure of form II and the corresponding $R_H$ value (Figure 3A). Full-length ESCRT-II was modeled by positioning the GLUE domain interactively so as to obtain agreement with between the calculated and experimental $R_H$ values (Figure 3A). The structure of the human ESCRT-II GLUE domain was obtained from PDB entry 2HTH (Alam et al., 2006).

### Pull-Down Assays

For GST-pull-downs, 50 μl gluthathione sepharose resin was prewashed with binding buffer (1X PBS). GST-tagged human VPC28 C-terminal domain (residues 123–220) was bound to the resin. Various purified constructs of human ESCRT-II complex were mixed with the GST-VPS28 CTD-bound resin for 30 min at room temperature. GST-bound resin was used as a negative control. The beads were then washed three times with 1X PBS. and the bound proteins were analyzed by SDS-PAGE.

### Liposome-Binding Experiments

The synthetic lipids used in this study were all purchased from Avanti Polar Lipids except for PI(3)P, which was purchased from Echelon. All liposomes contain 0.5% of a dye, lissamine rhodamine B, for quantitation of the liposomes. The liposomes were prepared at a total lipid concentration of 1 mg/ml by evaporating the solvent from the desired lipid mixture using a nitrogen stream. The dried lipids were resuspended in 150 μl 0.3 M sucrose, and the solution was incubated at room temperature under nitrogen for 1 hr with periodic vortexing; 1 ml water was added and the sample was sedimented in an ultracentrifuge at 128,000 × g for 30 min at 4°C. The supernatant was removed, and the pellet was frozen and thawed three times in liquid nitrogen. The pellet was dissolved in 1 ml buffer A (20 mM HEPES [pH 7.4] and 150 mM NaCl) and extruded 10 times through a 0.1 μm filter. For binding experiments, 100 μg liposomes were mixed with 80 μg protein and were brought up to a total volume of 200 μl with buffer A, incubated at room temperature for 30 min, and sedimented at 128,000 × g at 4°C for 30 min. The pellet was washed once with 200 μl buffer A and again sedimented for 30 min. Samples of the supernatant (10 μl) and pellet were analyzed by SDS-PAGE. The intensities of bands in the SDS-PAGE gels were measured using the LabWorks 5.6 program (UVP).

### Plasmid Construction and Yeast Strains

The *vps22*Δ *vps36*Δ strain was prepared by replacing the *VPS36* gene with a nourseothrisin resistance gene from a *vps22*Δ strain by homologous recombination. The *vps4*Δ *vps22*Δ *vps36*Δ strain was made by homologous recombination between the VPS4 and URA3 genes in the *vps22*Δ *vps36*Δ strain. The complete expression cassette of Vps22 and the open reading frame of Vps36 were amplified from yeast genomic DNA and cloned into YCplac111 and pRS413MET25 vectors, respectively. The N-teminal 30 amino acid deletion of Vps22 and the R89A and R261A mutations of Vps36 were introduced by Quickchange mutagenesis (Stratagene). DNA coding for green fluorescent protein (GFP) was fused to the 3′ end of the vps22 cassette using PCR, and the PCR product was cloned to the YCplac111 vector. Plasmids encoding *VPS22* and *VPS36* genes, and the pGO45 vector, were transformed to wild-type and mutant strains. The following yeast strains were used: BY4741 (MAT**a** *his3Δ1 leu2Δ0 met15Δ0 ura3Δ0*), BY4741 *vps22Δ::KanR*, BY4741 *vps36Δ::KanR*, BY4741 *vps22Δ::KanR vps36Δ::NATR*, BY4741 *vps22Δ::KanR vps36Δ::NATR vps4Δ::URA3*.

### Microscopy

Yeast strains expressing the appropriate alleles were harvested at an A660 of 0.4–0.6, labeled with FM4-64 for vacuolar membrane staining (Vida and Emr, 1995). Uptake of FM4-64 by live cells was performed at 30°C for 1 hr, after which cells were resuspended in selection media and incubated for 30 min at 30°C. Visualization of cells was performed on an LSM510 fluorescence microscope (Carl Zeiss MicroImaging) equipped with fluorescein isothiocyanate (FITC) and rhodamine filters and captured with a digital camera.

## ACCESSION NUMBERS

Crystallographic coordinates have been deposited in the Protein Data Bank with accession codes 3CUQ for crystal form I and 2ZME for form II.

## SUPPLEMENTAL DATA

Supplemental Data include four figures and are available with this article online at http://www.developmentalcell.com/cgi/content/full/14/6/902/DC1/.

## ACKNOWLEDGMENTS

We thank to Will Prinz and Beverly Wendland for technical advice on yeast experiments, W.P. and Greg Odorizzi for providing plasmids and yeast strains, Boris Baibakov for technical assistance on yeast microscopy imaging, the SER-CAT staff for user support at the Advanced Photon Source (APS), and B.W. for comments on the manuscript. Use of the APS was supported by the US DOE, Basic Energy Sciences, Office of Science, under Contract No.W-31-109-Eng-38. This research was supported by NIH intramural support, NIDDK and IATAP.

Received: January 25, 2008
Revised: March 31, 2008
Accepted: April 18, 2008
Published: June 9, 2008

## REFERENCES

Alam, S.L., Sun, J., Payne, M., Welch, B.D., Black, B.K., Davis, D.R., Meyer, H.H., Emr, S.D., and Sundquist, W.I. (2004). Ubiquitin interactions of NZF zinc fingers. EMBO J. *23*, 1411–1421.

Alam, S.L., Langelier, C., Whitby, F.G., Koirala, S., Robinson, H., Hill, C.P., and Sundquist, W.I. (2006). Structural basis for ubiquitin recognition by the human ESCRT-II EAP45 GLUE domain. Nat. Struct. Mol. Biol. *13*, 1029–1030.

Babst, M. (2005). A protein's final ESCRT. Traffic *6*, 2–9.

Babst, M., Katzmann, D.J., Snyder, W.B., Wendland, B., and Emr, S.D. (2002). Endosome-associated complex, ESCRT-II, recruits transport machinery for protein sorting at the multivesicular body. Dev. Cell *3*, 283–289.

Bieniasz, P.D. (2006). Late budding domains and host proteins in enveloped virus release. Virology *344*, 55–63.

Bowers, K., Piper, S.C., Edeling, M.A., Gray, S.R., Owen, D.J., Lehner, P.J., and Luzio, J.P. (2006). Degradation of endocytosed epidermal growth factor and virally ubiquitinated major histocompatibility complex class I is independent of mammalian ESCRTII. J. Biol. Chem. *281*, 5094–5105.

Brunger, A.T., Adams, P.D., Clore, G.M., DeLano, W.L., Gros, P., Grosse-Kunstleve, R.W., Jiang, J.S., Kuszewski, J., Nilges, M., Pannu, N.S., et al. (1998). Crystallography & NMR system: A new software suite for macromolecular structure determination. Acta Crystallogr. D Biol. Crystallogr. *54*, 905–921.

Carlton, J.G., and Martin-Serrano, J. (2007). Parallels between cytokinesis and retroviral budding: a role for the ESCRT machinery. Science *316*, 1908–1912.

CCP4 (Collaborative Computational Project, Number 4) (1994). The CCP4 suite: programs for protein crystallography. Acta Crystallogr. A *50*, 760–763.

De Domenico, I., Ward, D.M., Langelier, C., Vaughn, M.B., Nemeth, E., Sundquist, W.I., Ganz, T., Musci, G., and Kaplan, J. (2007). The molecular mechanism of hepcidin-mediated ferroportin down-regulation. Mol. Biol. Cell *18*, 2569–2578.

Emsley, P., and Cowtan, K. (2004). Coot: model-building tools for molecular graphics. Acta Crystallogr. D Biol. Crystallogr. *60*, 2126–2132.

Garcia de la Torre, J., Huertas, M.L., and Carrasco, B. (2000). Calculation of hydrodynamic properties of globular proteins from their atomic-level structure. Biophys. J. *78*, 719–730.

Gill, D.J., Teo, H., Sun, J., Perisic, O., Veprintsev, D.B., Emr, S.D., and Williams, R.L. (2007). Structural insight into the ESCRT-I/-II link and its role in MVB trafficking. EMBO J. *26*, 600–612.

Herz, H.M., Chen, Z., Scherr, H., Lackey, M., Bolduc, C., and Bergmann, A. (2006). vps25 mosaics display non-autonomous cell survival and overgrowth, and autonomous apoptosis. Development *133*, 1871–1880.

Hierro, A., Sun, J., Rusnak, A.S., Kim, J., Prag, G., Emr, S.D., and Hurley, J.H. (2004). Structure of the ESCRT-II endosomal trafficking complex. Nature *431*, 221–225.

Hirano, S., Suzuki, N., Slagsvold, T., Kawasaki, M., Trambaiolo, D., Kato, R., Stenmark, H., and Wakatsuki, S. (2006). Structural basis of ubiquitin recognition by mammalian Eap45 GLUE domain. Nat. Struct. Mol. Biol. *13*, 1031–1032.

Hoover, D.M., and Lubkowski, J. (2002). DNAWorks: an automated method for designing oligonucleotides for PCR-based gene synthesis. Nucleic Acids Res. *30*, e43.

Hurley, J.H. (2008). ESCRT Complexes and the Biogenesis of Multivesicular Bodies. Curr. Opin. Cell Biol. *20*, 4–11.

Irion, U., and St Johnston, D. (2007). bicoid RNA localization requires specific binding of an endosomal sorting complex. Nature *445*, 554–558.

Jones, T.A., Zou, J.Y., Cowan, S.W., and Kjeldgaard, M. (1991). Improved methods for building protein models in electron-density maps and the location of errors in these models. Acta Crystallogr. A *47*, 110–119.

Kamura, T., Burian, D., Khalili, H., Schmidt, S.L., Sato, S., Liu, W.J., Conrad, M.N., Conaway, R.C., Conaway, J.W., and Shilatifard, A. (2001). Cloning and characterization of ELL-associated proteins EAP45 and EAP20. a role for yeast EAP-like proteins in regulation of gene expression by glucose. J. Biol. Chem. *276*, 16528–16533.

Kostelansky, M.S., Sun, J., Lee, S., Kim, J., Ghirlando, R., Hierro, A., Emr, S.D., and Hurley, J.H. (2006). Structural and functional organization of the ESCRT-I trafficking complex. Cell *125*, 113–126.

Kostelansky, M.S., Schluter, C., Tam, Y.Y.C., Lee, S., Ghirlando, R., Beach, B., Conibear, E., and Hurley, J.H. (2007). Molecular architecture and functional model of the complete yeast ESCRT-I heterotetramer. Cell *129*, 485–498.

Langelier, C., von Schwedler, U.K., Fisher, R.D., De Domenico, I., White, P.L., Hill, C.P., Kaplan, J., Ward, D., and Sundquist, W.I. (2006). Human ESCRT-II complex and its role in human immunodeficiency virus type 1 release. J. Virol. *80*, 9465–9480.

Malerod, L., Stuffers, S., Brech, A., and Stenmark, H. (2007). Vps22/EAP30 in ESCRT-II mediates endosomal sorting of growth factor and chemokine receptors destined for lysosomal degradation. Traffic *8*, 1617–1629.

Martin-Serrano, J., Yarovoy, A., Perez-Caballero, D., and Bieniasz, P.D. (2003). Divergent retroviral late-budding domains recruit vacuolar protein sorting factors by using alternative adaptor proteins. Proc. Natl. Acad. Sci. USA *100*, 12414–12419.

Morita, E., Sandrin, V., Chung, H.Y., Morham, S.G., Gygi, S., Rodesch, C.K., and Sundquist, W.I. (2007). Human ESCRT and ALIX proteins interact with proteins of the midbody and function in cytokinesis. EMBO J. *26*, 4215–4227.

Nickerson, D.P., Russell, D.W., and Odorizzi, G. (2007). A concentric circle model of multivesicular body cargo sorting. EMBO Rep. *8*, 644–650.

Pineda-Molina, E., Belrhali, H., Piefer, A.J., Akula, I., Bates, P., and Weissenhorn, W. (2006). The crystal structure of the C-terminal domain of Vps28 reveals a conserved surface required for Vps20 recruitment. Traffic *7*, 1007–1016.

Prag, G., Watson, H., Kim, Y.C., Beach, B.M., Ghirlando, R., Hummer, G., Bonifacino, J.S., and Hurley, J.H. (2007). The Vps27/Hse1 complex is a GAT domain-based scaffold for ubiquitin-dependent sorting. Dev. Cell *12*, 973–986.

Progida, C., Spinosa, M.R., De Luca, A., and Bucci, C. (2006). RILP interacts with the VPS22 component of the ESCRT-II complex. Biochem. Biophys. Res. Commun. *347*, 1074–1079.

Progida, C., Malerod, L., Stuffers, S., Brech, A., Bucci, C., and Stenmark, H. (2007). RILP is required for the proper morphology and function of late endosomes. J. Cell Sci. *120*, 3729–3737.

Saksena, S., Sun, J., Chu, T., and Emr, S.D. (2007). ESCRTing proteins in the endocytic pathway. Trends Biochem. Sci. *32*, 561–573.

Slagsvold, T., Aasland, R., Hirano, S., Bache, K.G., Raiborg, C., Trambaiano, D., Wakatsuki, S., and Stenmark, H. (2005). Eap45 in mammalian ESCRT-II binds ubiquitin via a phosphoinositide-interacting GLUE domain. J. Biol. Chem. *280*, 19600–19606.

Slagsvold, T., Pattni, K., Malerod, L., and Stenmark, H. (2006). Endosomal and non-endosomal functions of ESCRT proteins. Trends Cell Biol. *16*, 317–326.

Teo, H., Perisic, O., Gonzalez, B., and Williams, R.L. (2004). ESCRT-II, an endosome-associated complex required for protein sorting: Crystal structure and interactions with ESCRT-III and membranes. Dev. Cell *7*, 559–569.

Teo, H., Gill, D.J., Sun, J., Perisic, O., Veprintsev, D.B., Vallis, Y., Emr, S.D., and Williams, R.L. (2006). ESCRT-I core and ESCRT-II GLUE domain structures reveal role for GLUE in linking to ESCRT-I and membranes. Cell *125*, 99–111.

Terwilliger, T.C. (2000). Maximum-likelihood density modification. Acta Crystallogr. D Biol. Crystallogr. *56*, 965–972.

Terwilliger, T.C., and Berendzen, J. (1999). Automated MAD and MIR structure solution. Acta Crystallogr. D Biol. Crystallogr. *55*, 849–861.

Thompson, B.J., Mathieu, J., Sung, H.H., Loeser, E., Rorth, P., and Cohen, S.M. (2005). Tumor suppressor properties of the ESCRT-II complex component vps25 in *Drosophila*. Dev. Cell *9*, 711–720.

Vaccari, T., and Bilder, D. (2005). The *Drosophila* tumor suppressor vps25 prevents nonautonomous overproliferation by regulating Notch trafficking. Dev. Cell *9*, 687–698.

Vida, T.A., and Emr, S.D. (1995). A new vital stain for visualizing vacuolar membrane dynamics and endocytosis in yeast. J. Cell Biol. *128*, 779–792.

von Schwedler, U.K., Stuchell, M., Muller, B., Ward, D.M., Chung, H.Y., Morita, E., Wang, H.E., Davis, T., He, G.P., Cimbora, D.M., et al. (2003). The protein network of HIV budding. Cell *114*, 701–713.

Wang, T., and Hong, W. (2006). RILP interacts with VPS22 and VPS36 of ESCRT-II and regulates their membrane recruitment. Biochem. Biophys. Res. Commun. *350*, 413–423.

Williams, R.L., and Urbe, S. (2007). The emerging shape of the ESCRT machinery. Nat. Rev. Mol. Cell Biol. *8*, 355–368.

Yorikawa, C., Shibata, H., Waguri, S., Hatta, K., Horii, M., Katoh, K., Kobayashi, T., Uchiyama, Y., and Maki, M. (2005). Human CHMP6, a myristoylated ESCRT-III protein, interacts directly with an ESCRT-II component EAP20 and regulates endosomal cargo sorting. Biochem. J. *387*, 17–26.

**Developmental Cell *14***

# Supplemental Data

# Integrated Structural Model and Membrane Targeting Mechanism of the Human ESCRT-II Complex

**Young Jun Im and James H. Hurley**

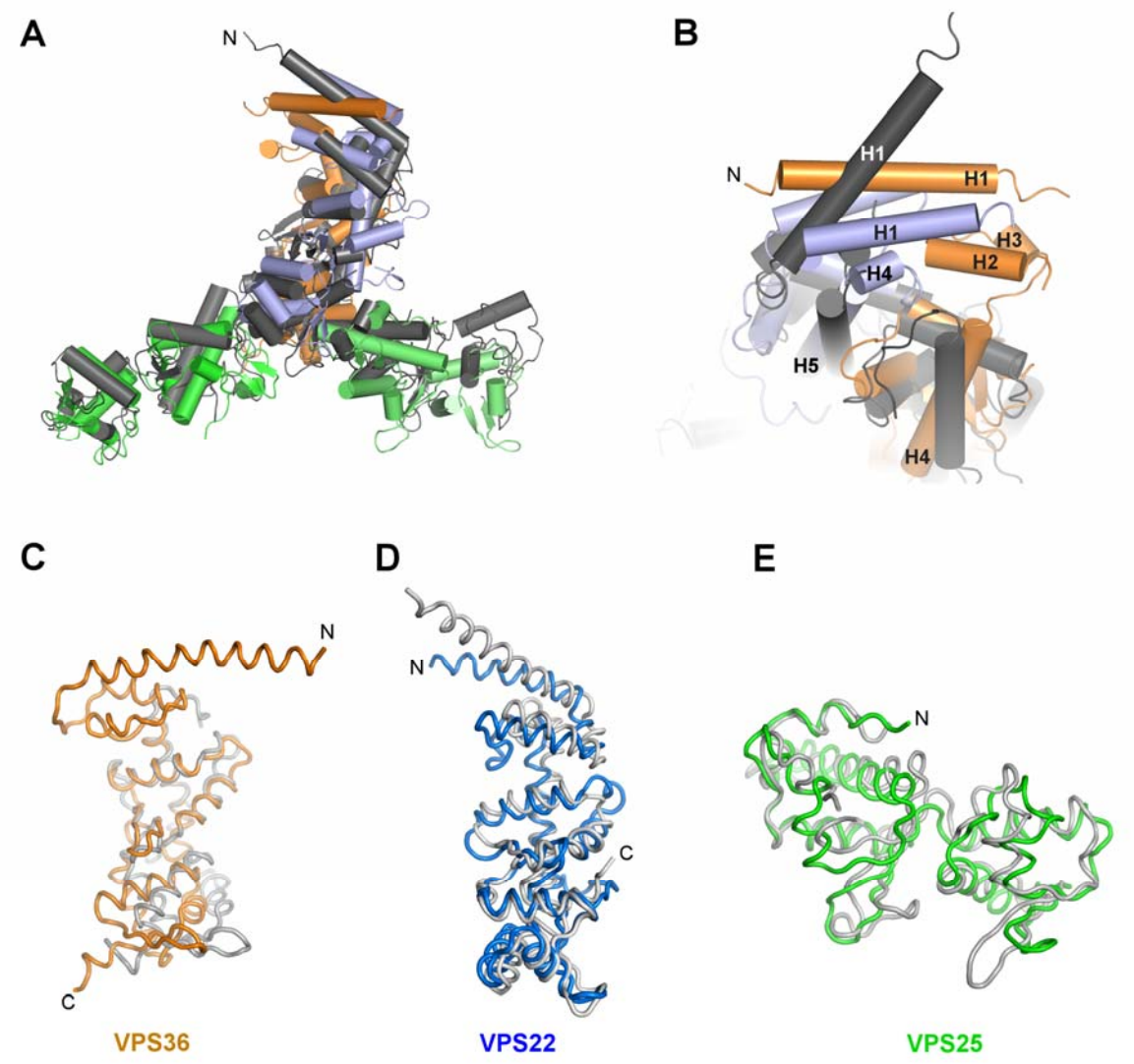


**Figure S1.** Comparison of Human and Yeast ESCRT-II Structures

(A) Overall structure superposition of human and yeast ESCRT-II cores. Human ESCRT-II was shown in the same colors as in Fig. 1, and yeast ESCRT-II in dark-gray. Sequence

identities of VPS22, 25, and 36 in human and yeast are 33, 26, and 12% respectively. (B) Superposition of the N-terminal HD region. (C-E) Superpositions of individual subunits, colored as in (A).

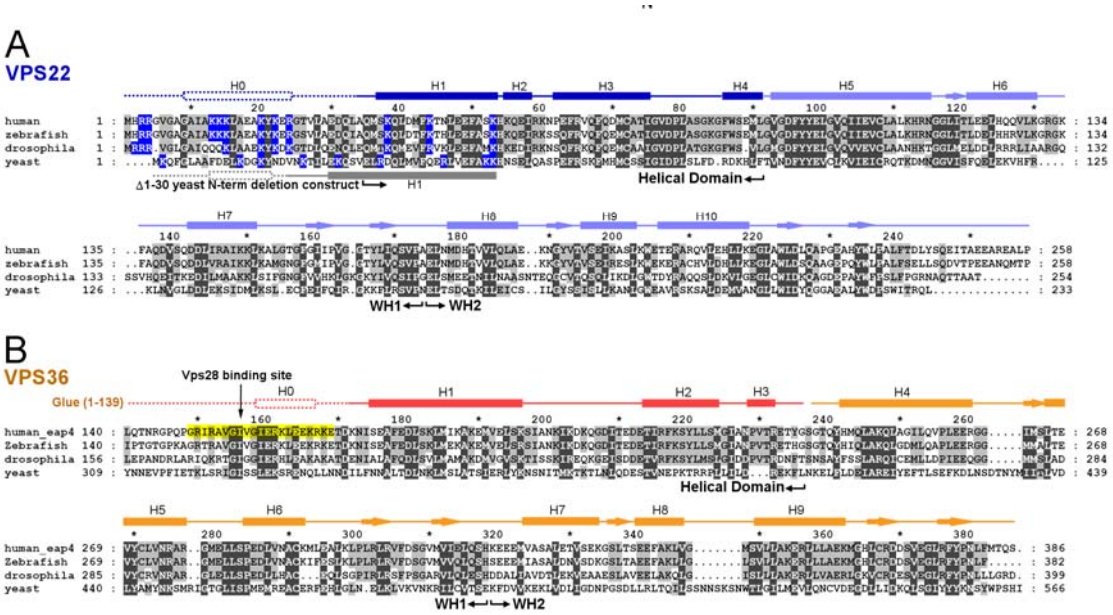


**Figure S2.** Sequence Alignments of (A) Human VPS22 and (B) Human VPS36 and Their Orthologs in Zebrafish, *Drosophila*, and Yeast

The secondary structure elements of human ESCRT-II are shown in bars for helices and arrows for β-strands. Predicted secondary structure elements from PredictProtein Server (Rost and Liu, 2003) are shown in dashed lines. Secondary structure elements of yeast Vps22 were shown in gray.

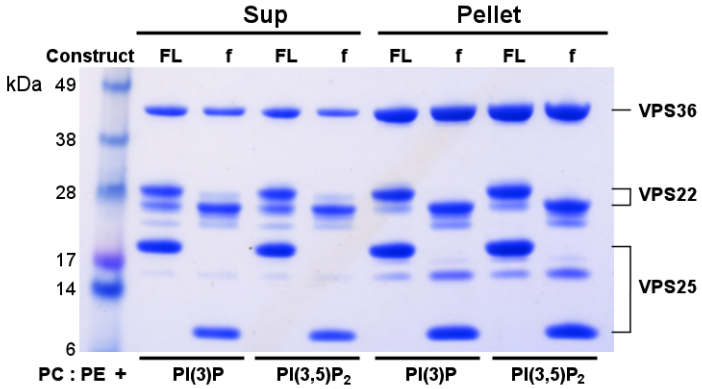


**Figure S3.** Alternative Models for the Conformation of Intact ESCRT-II

The calculated Stokes radius $R_H$ is shown for various models. (A) An alternative model consistent with the experimental $R_H$, in which the GLUE domain contacts the HD region,

but the precise conformation differs from that shown in Fig. 3B. (B, C) Two alternative models in which the GLUE domain packs against the WH domains of the ESCRT-II core. These conformations have calculated $R_H$ values that are substantially lower than the experimental value. (D) An alternative model in which the GLUE domain does not make direct contact with the ESCRT-II core. This and other such conformations lead to calculated $R_H$ values that are substantially higher than the experimental value.

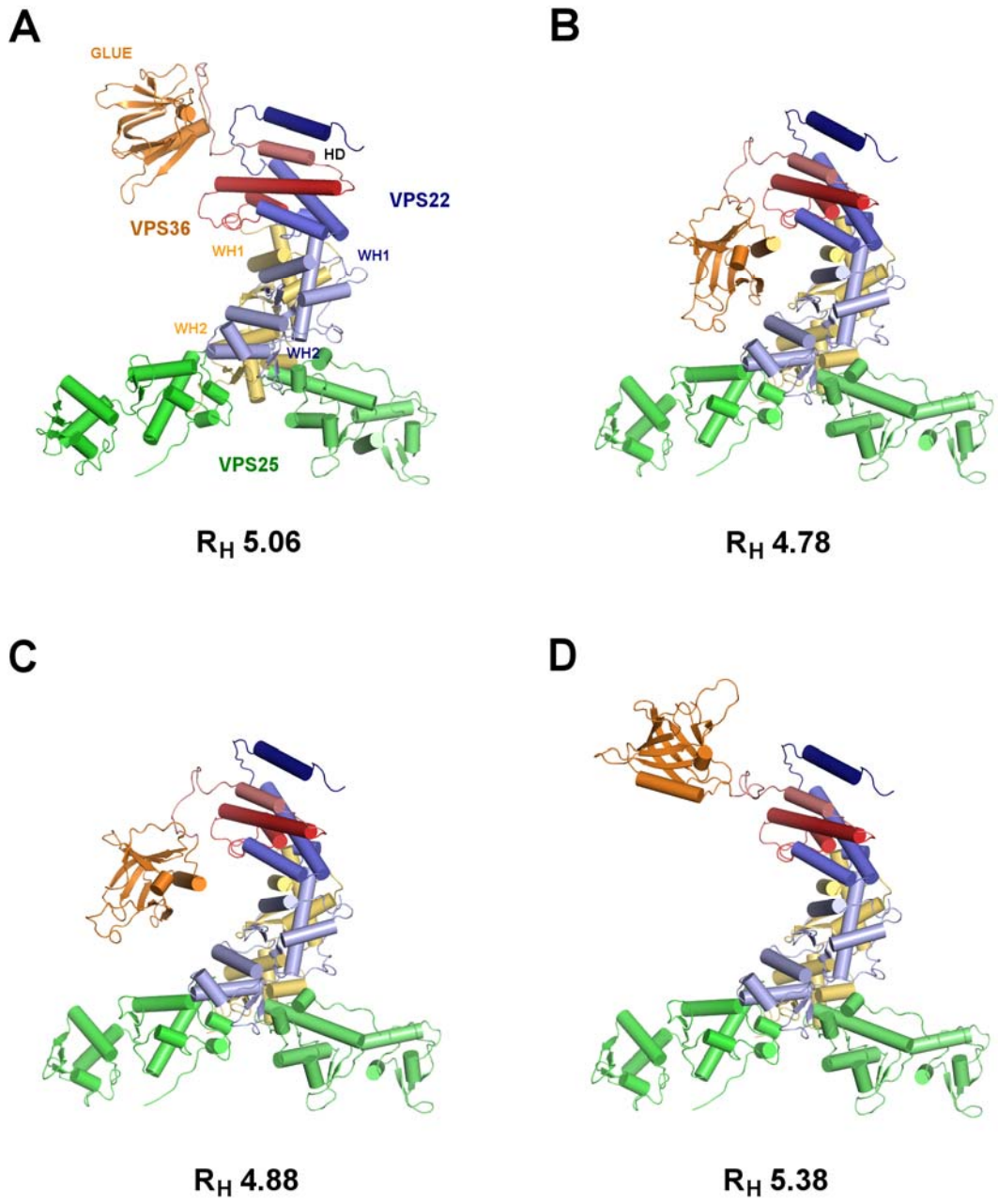


**Figure S4.** Intact and "Pseudo-Intact" ESCRT-II Binding to Liposomes

“FL” designates full-length ESCRT-II, while “f” designates construct f (Fig. 3C) used as the pseudo-intact ESCRT-II in liposome binding studies.

**Supplemental Reference**

Rost, B., and Liu, J. F. (2003). The PredictProtein server. Nucleic Acids Res. *31*, 3300-3304.